Nano Research 2017, 10(11): 3621–3628
DOI 10.1007/s12274-017-1539-x
Research Article

ISSN 1998-0124
CN 11-5974/O4

Mild metal-organic-gel route for synthesis of stable sub-5-nm metal-organic framework nanocrystals

Yue Qi[§], Chun-Ting He[§], Juntao Lin, Shuping Lin, Jin Liu, Jinghong Huang, Wei Xue, Guicheng Yu, Hsiu-Yi Chao, Yexiang Tong, and Zhengping Qiao (✉)

MOE Key Laboratory of Bioinorganic and Synthetic Chemistry, School of Chemistry, Sun Yat-Sen University, Guangzhou 510275, China
[§] *Yue Qi and Chun-Ting He contributed equally to this work.*

Received: 22 December 2016
Revised: 13 February 2017
Accepted: 14 February 2017

KEYWORDS
metal-organic gel,
metal-organic frameworks,
nanoparticles,
liquid adsorption

ABSTRACT

Nanoscale metal-organic frameworks (NMOFs) have attracted increased attention in recent years for miniaturized and/or biological applications. However, the synthesis of ultrasmall NMOFs with good stability is a great challenge. In this study, sub-5-nm nano-HKUST-1 was prepared for the first time via a mild metal-organic gel route without surfactants or capping agents. Controlling the gelation process via anion–ligand self-assembly is the key to the formation of NMOFs. The Tyndall effect, zeta potential, and liquid adsorption indicated strong stability of the obtained nano-HKUST-1, even in water. Adsorption experiments were performed using different dyes (crystal violet and methylene blue) to demonstrate the size-dependent adsorption thermodynamics and kinetics of this famous MOF. The results of this study provide new insights regarding the synthesis of NMOFs and their efficient applications.

1 Introduction

Metal-organic frameworks (MOFs) have attracted considerable attention in the past two decades owing to their large internal surface areas, widely tunable compositions, and regular pore structures [1–4]. Both MOFs and conventional nanomaterials exhibit exceptionally large specific surface areas, which are due to the high porosity and small size, respectively. The rational combination of these two features can yield significant absorptivity, which is useful for identifying new functional sorbents [5, 6]. Compared with their bulk crystals, nanoscale MOFs (NMOFs) have attracted less attention, although they have exhibited great importance for many applications, such as enhancing ethylene separation [7], upconversion [8], drug delivery [9], and light harvesting [10]. The lack of attention is due to the dearth of effective strategies for synthesizing well-defined NMOFs with exceptional thermal/chemical stabilities. Under general reaction conditions (e.g., hydrothermal or solution diffusion), the organic anions and the metal cations tend to rapidly crystallize into bulk MOFs through the consecutive epitaxial growth and/or oriented attachment induced by surface

Address correspondence to cesqzp@mail.sysu.edu.cn

intension or fast agglomeration [11, 12]. Thus far, the addition of surfactants or other capping agents is the most common method for reducing the size of MOF crystals. However, such additives are difficult to remove, especially those in the cavities of MOFs [13–15]. Recently, ultrasmall Al(III)-based MOF particles (10–20 nm) were obtained using a metal-organic aerogel method; however, heating was needed to control the gelation or crystallization, and it was difficult to further reduce the sizes [16]. Similarly, the metal-organic gel (MOG) process, which is widely used for the synthesis of traditional inorganic nanocrystals (such as TiO_2 and ZnO), is an effective method for controlling the coordination equilibria in MOF growth. Here, the tiny crystals can be separated and protected by the non-crystallographic scaffolding branches connected with other supramolecular interactions (e.g., hydrogen bonding or π–π stacking) [17, 18]. More importantly, the epitaxies of the nanocrystals are inhibited when the coordination is perturbed by other competing interactions during the gelation process, yielding homogeneous and ultrasmall crystalline particles. Nevertheless, the synthesis of NMOFs with particle sizes < 5 nm is a great challenge because of the large cell sizes (usually > 1 nm) and highly open structures [9, 19, 20]. Moreover, the adsorption behaviors, especially the liquid-phase capture of such ultramicroscopic porous particles, remain unknown [21–24].

In this study, by using $Cu_3(BTC)_2$ (H_3BTC = 1,3,5-benzenetricarboxylic acid) (HKUST-1) as an example, we for the first time demonstrated a mild MOG route for obtaining NMOFs with particle sizes < 5 nm. The process can be performed at room temperature without additional reagents like trimethylamine, which is commonly used as a trigger and causes an unexpected auxiliary effect [25].

Compared with previous synthesis methods [25, 26], the reaction time was ultrashort (< 2 min, followed by a 12-h treatment for removing guest molecules), and systematic experiments revealed that the solvent, relative quantity of the reactants, ultrasonic time, and temperature could be varied over a wide range. Furthermore, the Tyndall effect, zeta potential, and absorption of dye indicated the high stability of the HKUST-1 nanoparticles (NPs), even in water. Using powder X-ray diffraction (PXRD), confocal microscopy, and molecular simulations, the adsorption behaviors—including the adsorption kinetics—were investigated in detail. As the crystal sizes decreased from the microscale to the nanoscale, the absorption quantity of pore-blocking molecules (crystal violet, CV) and the rate constant of pore-admission molecule (methylene blue, MB) increased by factors of three and four, respectively. Thus, the rate exhibited little size-dependence for the former dye molecule, and the quantity exhibited little size-dependence for the latter dye molecule. The proposed MOG route can be extended to the synthesis of other NMOFs that have been previously reported or are newly developed.

2 Results and discussion

Figures 1 and 2 show the composition and morphology, respectively, of the as-synthesized HKUST-1 NPs, HKUST-1 gel (MOG), and HKUST-1 microparticles (μPs). PXRD, Raman spectroscopy [27], and ^1H nuclear magnetic resonance (NMR) supported the formation of HKUST-1.

The TEM images indicate that the MOG and the NPs had similar monodisperse morphologies comprising 2–5 nm spherical particles. To our knowledge, this is the smallest NMOF reported thus far. Analysis

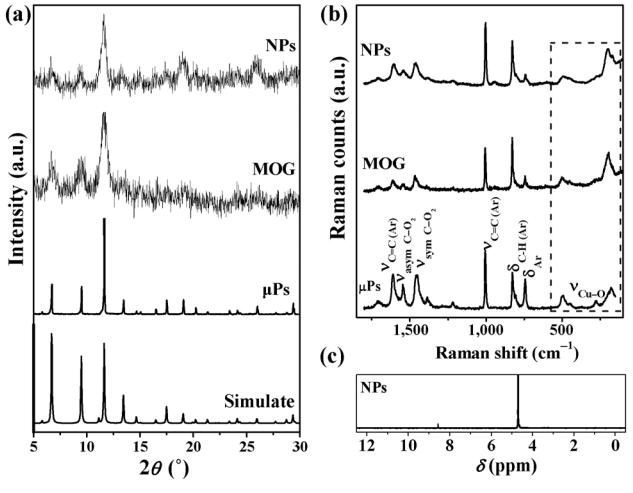

Figure 1 Composition characterization of the as-synthesized NPs, MOG, and μPs. (a) PXRD patterns for the samples and a simulated PXRD pattern for a single crystal; (b) Raman spectra for samples; (c) ^1H NMR of NPs dissolved in deuterium oxide and a small amount of deuterium chloride. The peaks at 4.7 and ~ 8.8 ppm correspond to deuterium oxide and the three identical protons of the H_3BTC ligand, respectively [28].

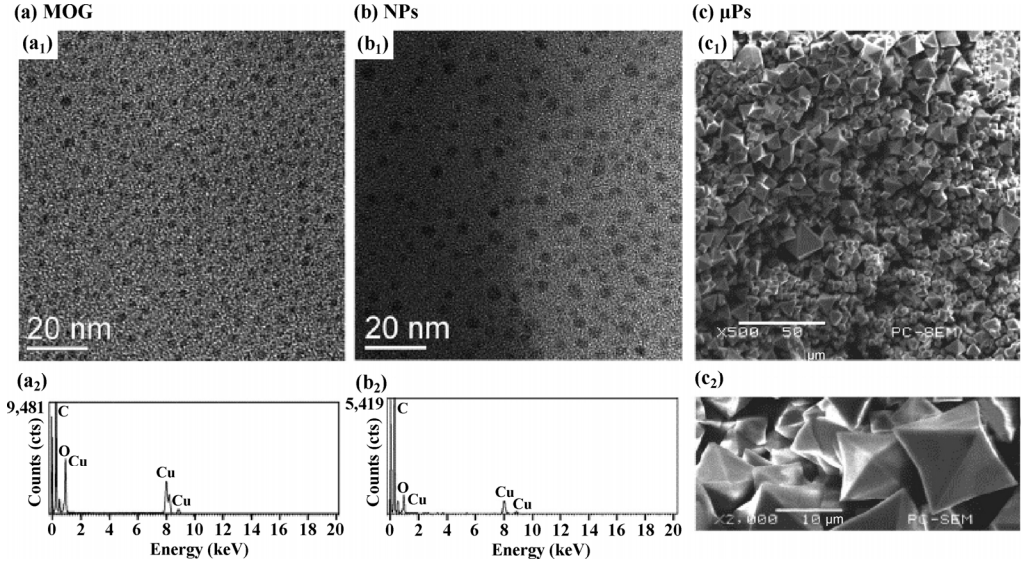

Figure 2 Morphology characterizations of the products. TEM images of the (a_1) MOG and (b_1) NPs, EDS results for the (a_2) MOG and (b_2) NPs, and (c_1) and (c_2) SEM images of the μPs.

of the MOG via scanning transmission electron microscopy (STEM) revealed that the monodispersion was probably due to the hydrogen-bonding networks between the particles. Energy-dispersive X-ray spectroscopy (EDS) confirmed that the as-synthesized MOG and NPs consisted of copper, carbon, and oxygen. SEM indicated that the as-prepared μPs were concave octahedra with particle sizes of 5–20 μm. Details regarding the preparation of the NPs and μPs are shown in the Electronic Supplementary Material (ESM). The transformation of the products is shown in Fig. 3. HKUST-1 colloids (MOC) were formed immediately after 2 min of ultrasonication. Reversible transformation of the sol–gel was easily accomplished via centrifugation/solvent evaporation (step 1) and dilution with ethanol (step 2). By heating the MOG at 200 °C for 12 h in N_2, NP powder was obtained (step 3). The NPs and their suspension were reversibly transformed via ultrasonication in ethanol (step 4) and dried (step 5). The Tyndall effect was observed in the MOC and the suspension of NPs, indicating the formation of colloids or NPs in the fine suspension.

In our approach, MOG was necessary for the preparation of the NPs. To gain insight into the key factor for the formation of the MOG, the basic parameters for the preparation were studied: the copper sources, solvents, relative quantity of the reactants, ultrasonic time, and temperature. The results showed that solvents and copper sources were crucial, whereas the other parameters could be changed over wide ranges (Figs. S1–S5 in the ESM). Regarding the copper source, copper acetate was the key factor. The anion–ligand self-assembly (ALSA) arising from the hydrogen bonds between the CH_3COO^- and BTC^{3-} was crucial because it crosslinked the particle species into networks; thus, no gel or NPs formed when the copper source was changed to $Cu(NO_3)_2$. The effect of the solvent was investigated using dimethyl sulfoxide (DMSO),

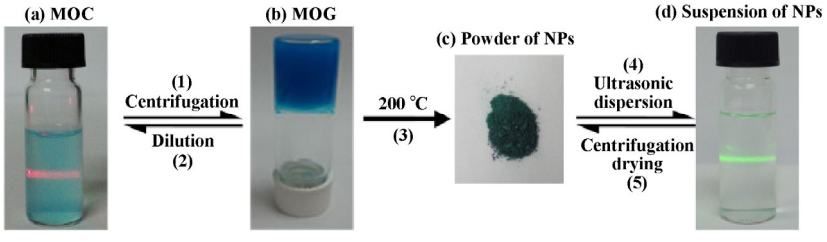

Figure 3 Transformation of the (a) HKUST-1 colloids (MOC), (b) HKUST-1 gel (MOG), (c) powder of HKUST-1 NPs, and (d) suspension of HKUST-1 NPs. (a) and (d) show the Tyndall effect.

acetonitrile, ethanol, water, and dimethyl formamide (DMF). NPs were obtained in DMSO, acetonitrile, ethanol, DMF, and water. The introduction of water in the reactions increased the size of the crystal. On one hand, the water reduced the solubility of the organic ligands in the solvents. On the other hand, the ALSA process was interrupted by the strong hydrogen-bond donors/acceptors.

The components of the MOG was investigated to clarify the effect of the copper source. STEM (Fig. 4) of the MOG revealed copper both in and around the particles. In general, the formation of the MOG occurred in three stages: 1) the polymerization of the precursors (coordination of organic ligands with metal ions), forming NPs; 2) the growth/aggregation of the NPs; and 3) the crosslinking of the particle species into networks [29, 30]. According to the STEM images, the copper observed in the particles was from the HKUST-1 crystals, and that around the particles was from the precursors that had not formed particles yet.

Interestingly, this MOG route for obtaining NMOFs can be extended to $[Co_3(BDC)_3(DMF)_2(H_2O)_2]_2$ nanorods, $[Ni_3(BDC)_3(DMF)_2(H_2O)_2]_2$, and $Zn_4O(BDC)_3(DMF)_8$ NPs (H_2BDC = 1,4–dicarboxylbenzene) (Fig. S6 in the ESM). In particular, $[Ni_3(BDC)_3(DMF)_2(H_2O)_2]_2$ is isomorphous to $[Co_3(BDC)_3(DMF)_2(H_2O)_2]_2$ and was reported first.

Because the physical properties of suspensions and colloids greatly depend on the properties of the particle–liquid interface, the zeta potentials of the NPs and μPs in ethanol were measured. They were −61.64 and −31.21 mV for the NPs and μPs, respectively. The twofold increase in the zeta potential indicates the unexpectedly enhanced stability of the NPs, which may have been caused by the amorphous scaffolding buffered branches that covered the particles and protected them from the highly polar solvents, such as water molecules. The negative values indicate good adsorption properties for dye with a positive charge.

Despite the fascinating characteristics of MOFs, such as gas storage [31, 32], separation [2, 33], sensing [34, 35], and catalysis [36, 37], their applications in liquid-phase adsorption and separation are still at an early stage [21–24]. Therefore, CV and MB were selected to investigate the effects of the particle size of HKUST-1 and the shape of the dye. These two dyes have the same ending group, $–NH(CH_3)_2$ (6.1 Å-in-width, 4.2 Å-in-thickness) but different shapes. The shape of CV resembles a fan, and that of MB is similar to a cuboid. According to the size of the pore window for HKUST-1 (6.5 Å in diameter), the fan-like CV was plugged on the surface of the crystals, whereas the MB entered the interior of the crystals. This nuance is shown in Fig. 5.

The porosity was confirmed by N_2-sorption measurements, which yielded a typical type-I sorption isotherm with a saturated uptake of 268 cm^3/g (Brunauer–Emmett–Teller surface area of 992 m^2/g, corresponding to a pore volume of 0.419 cm^3/g, which is smaller than that calculated for the crystal structure of HKUST-1 (0.796 cm^3/g)). This is attributed to the poor crystallinity of the ultrasmall NPs and the

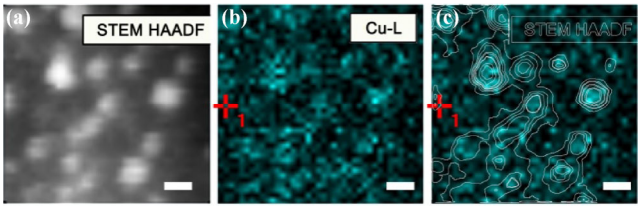

Figure 4 (a) High-angle annular dark-field (HAADF) STEM image obtained using an HAADF detector. (b) *In situ* elemental mapping of copper and (c) overlaid version of the elemental mapping showing the particle borderline (scale bar represents 4 nm).

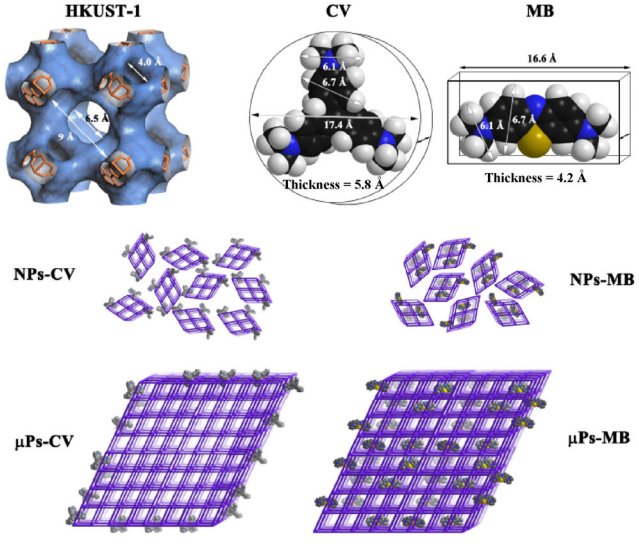

Figure 5 Schematic illustrations of the shape selectivity and adsorption dynamics. 1st line: dimensions of the pore windows in HKUST-1 and the dye molecules (CV and MB); 2nd and 3rd lines: schematic of the dye-adsorption processes (HKUST-1 NPs, HKUST-1 μPs).

existence of non-crystallographic scaffolding branches or substrates resulting from the ALSA gelation process. Nevertheless, the pore-size distribution exhibited a single peak around 8.6 Å (Fig. S7 in the ESM), which is consistent with the pore size (9.0 Å) measured according to the crystal structure. This supports the formation of HKUST-1.

Figure 6 shows the effect of the contact time on the adsorption of CV and MB onto the NPs and μPs. These kinetic data were analyzed using a pseudo-second order equation (Fig. S8 in the ESM), and the results are shown in Table S1 in the ESM. The results are summarized as follows. 1) When the initial concentration of dyes was lower, equilibrium was reached more quickly. The largest rate constant of second-order adsorption (k_2) within the range of our investigation was 0.045, 0.068, 0.43, and 0.10 g/(mg·min) for NPs-CV, μPs-CV, NPs-MB, and μPs-MB, respectively. 2) A higher initial concentration of dyes yielded a higher equilibrium adsorption capacity (Q_e). The maximum Q_e for NPs-CV, μPs-CV, NPs-MB, and μPs-MB was 242.29, 77.29, 221.73, and 220.37 mg/g, respectively, corresponding to 5.8, 1.8, 5.7, and 5.6 dye molecules per unit cell of HKUST-1, respectively. $Q_{e(NPs\text{-}CV)} >> Q_{e(\mu Ps\text{-}CV)}$, but $Q_{e(NPs\text{-}MB)} \approx Q_{e(\mu Ps\text{-}MB)}$, indicating the different adsorption modes. The Q_e for CV achieved in this study is the highest value reported thus far [38–41]. 3) In the μPs–dye system (Figs. 6(b) and 6(d)), the adsorption capacity at time t (Q_t) decreased after a period of contact, indicating that the structure of the MOFs collapsed and that the dyes were released. This accords with the typical instability of HKUST-1 in aqueous solutions [42]. The μPs were more stable in a more concentrated solution (0.20–1.00 mmol/L). In contrast, the NPs were stable in all of the solutions (Figs. 6(a) and 6(c)). This proves that highly stabile NMOFs can be obtained simply using the MOG method. In most MOFs, the chemical weak points are the metal–linker bonds, with hydrolysis yielding protonated linkers and hydroxide (or water)-ligated nodes [43]. The π–π stacking interaction and/or hydrophobic interactions between the dyes and the MOFs caused competition between the dye and water. Thus, a higher concentration of dye yielded more stable HKUST-1. When the particle sizes decreased to the nanoscale, the improved absorption of larger guest molecules shielded the Cu(II) ions from the water and significantly enhanced the stability.

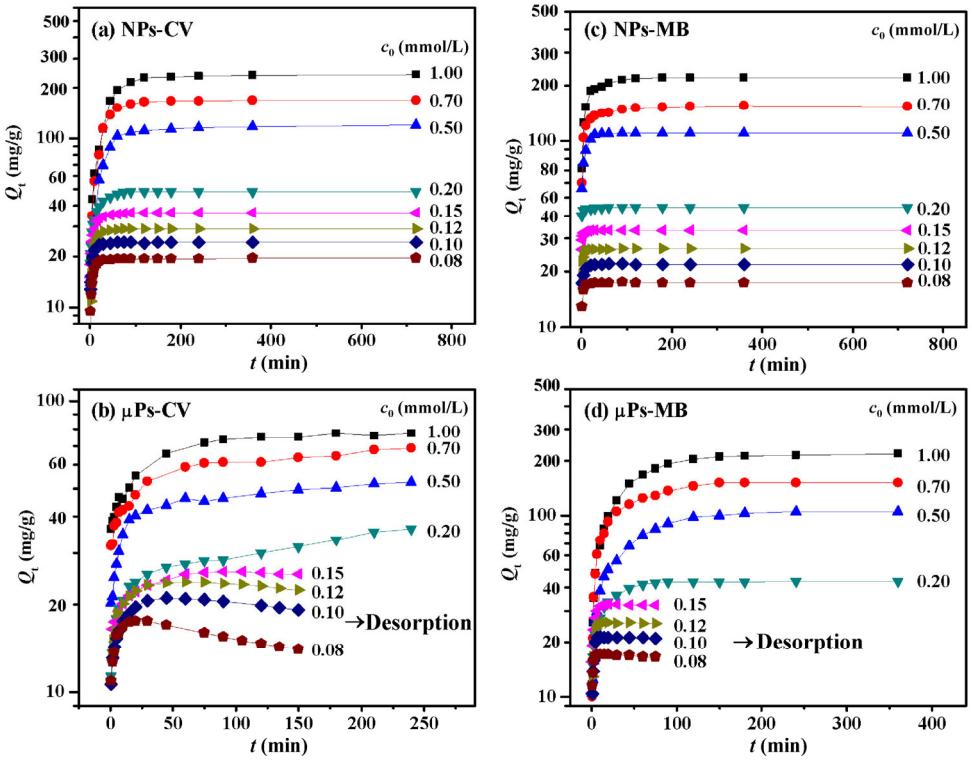

Figure 6 Effect of the contact time on the adsorption of CV and MB onto HKUST-1 NPs and μPs.

The experimental Q_e was analyzed using the Freundlich and Langmuir isotherm models, as shown in Fig. S9 in the ESM. The Freundlich isotherm provided better fitting of the experimental data than the Langmuir model, as indicated by the high correlation coefficient in the Freundlich equation. In the Freundlich model, the adsorption of the adsorbate occurs on a heterogeneous surface via multilayer sorption, and the adsorption capacity can increase with the adsorbate concentration.

XRD analysis was performed on the NPs and μPs after the absorption of the dyes to investigate the adsorption mechanism, and the results are shown in Fig. S10 in the ESM. Neither NPs-CV nor μPs-CV exhibited changes in the XRD patterns, indicating that the CV could not enter the lattice of HKUST-1; the absorption occurred only on the surface. However, the diffraction peak for both NPs-MB and μPs-MB shifted to a higher 2θ, indicating the lattice shrinkage of HKUST-1 after the absorption of MB. To explain this phenomenon, we performed molecular simulations of the MB adsorption in HKUST-1. As shown in Table S2 in the ESM, the lattice volumes were significantly reduced after the adsorption of either water (18,401 Å^3) or MB molecules (18,505 Å^3) compared with the previously empty framework containing only coordinated water molecules (18,529 Å^3). Moreover, if the adsorbate was a mixture of water and MB, the crystal lattice shrank to an even smaller volume (18,369 Å^3) because of the strong interactions between the host framework and the guest molecules, which was previously reported [44, 45].

Owing to the point-by-point excitation and detection, the distribution of the dyes was observed via confocal microscopy, especially for the inner part of the crystals. The results for the interaction between the μPs and CV/MB are shown in Fig. 7. The μPs were not octahedral, because of the grinding that occurred before the adsorption. Confocal luminescence images of the CV (Figs. 7(a_1)–7(a_3)) and MB (Figs. 7(b_1)–7(b_3)) indicate that CV existed in the edges or cracks of crystal but that MB existed throughout the entire crystal. This confirms the prediction shown in Fig. 5 and is consistent with the aforementioned results. To evaluate the regeneration and reusability of the NPs as an adsorbent, recycling dye-sorption experiments

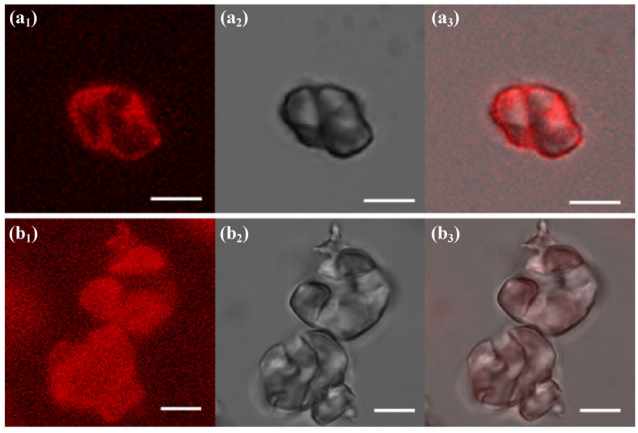

Figure 7 Confocal luminescence images of HKUST-1 μPs after interaction with (a) CV and (b) MB. (a_1) and (b_1) Distribution of the dye, (a_2) and (b_2) photos of the crystals, and (a_3) and (b_3) an overlaid version of the crystal/dye (scale bar represents 5 μm).

were performed, revealing that the capacities of CV on the NPs remained almost the same with increasing cycle numbers and that the CV removal efficiency remained above 95% even after 5 cycles (Fig. S11(a) in the ESM). Additionally, the crystal structure remained after each dye-sorption cycle (Fig. S11(b) in the ESM). These results confirm that the ultrasmall nano-HKUST-1 was exceptionally stable under recycling for CV sorption.

3 Conclusions

We prepared sub-5 nm nano-HKUST-1 from MOG for the first time, which was simply formed by mild anion–ligand self-assembly. This facile and general method can be employed for synthesizing other NMOFs and can lead to the formation of a new compound: $[Ni_3(BDC)_3(DMF)_2(H_2O)_2]_2$. The Tyndall effect, zeta potential, and absorption of dye indicated the high stability of the obtained NPs, even in water. The thermodynamics and kinetics of liquid adsorption were deeply studied, and the largest adsorption amount of CV to date was achieved. Additionally, the side-dependent adsorption modes were successfully clarified via molecular simulations, confocal microscopy, and XRD analysis. The effects of reducing the crystal sizes to the nanoscale were determined by the degree of matching between the molecular shape of the dye and the pore size of the MOFs: The Q_e increased by a

factor of three for CV, whereas the k_2 increased by a factor of four for MB. The results elucidate the synthesis of NMOFs, and the adsorption models with different scales can guide the effective use of NMOFs.

Acknowledgements

This work was supported by the National Natural Science Foundation of China (No. 21571193), Open Funds of the state key Laboratory of Rare Earth Resource Utilization (No. RERU2013012), Science Foundation of Guangdong Province (No. 2015A030312007) and National Postdoctoral Program for Innovative Talents (No. BX201600195).

Electronic Supplementary Material: Supplementary material (further details of the experiments, the kinetics study of dye adsorption, discussion of adsorption mechanism) is available in the online version of this article at https://doi.org/10.1007/s12274-017-1539-x.

References

[1] Sung Cho, H.; Deng, H. X.; Miyasaka, K.; Dong, Z. Y.; Cho, M.; Neimark, A. V.; Ku Kang, J.; Yaghi, O. M.; Terasaki, O. Extra adsorption and adsorbate superlattice formation in metal-organic frameworks. *Nature* **2015**, *527*, 503–507.

[2] Li, J. R.; Sculley, J.; Zhou, H. C. Metal-organic frameworks for separations. *Chem. Rev.* **2012**, *112*, 869–932.

[3] Silva, P.; Vilela, S. M. F.; Tomé, J. P. C.; Almeida Paz, F. A. Multifunctional metal-organic frameworks: From academia to industrial applications. *Chem. Soc. Rev.* **2015**, *44*, 6774–6803.

[4] Zhang, J. P.; Zhang, Y. B.; Lin, J. B.; Chen, X. M. Metal azolate frameworks: From crystal engineering to functional materials. *Chem. Rev.* **2012**, *112*, 1001–1033.

[5] He, C. T.; Jiang, L.; Ye, Z. M.; Krishna, R.; Zhong, Z. S.; Liao, P. Q.; Xu, J. Q.; Ouyang, G. F.; Zhang, J. P.; Chen, X. M. Exceptional hydrophobicity of a large-pore metal-organic zeolite. *J. Am. Chem. Soc.* **2015**, *137*, 7217–7223.

[6] Hou, C.; Zhao, G. F.; Ji, Y. J.; Niu, Z. Q.; Wang, D. S.; Li, Y. D. Hydroformylation of alkenes over rhodium supported on the metal-organic framework ZIF-8. *Nano Res.* **2014**, *7*, 1364–1369.

[7] Cadiau, A.; Adil, K.; Bhatt, P. M.; Belmabkhout, Y.; Eddaoudi, M. A metal-organic framework-based splitter for separating propylene from propane. *Science* **2016**, *353*, 137–140.

[8] Mahato, P.; Monguzzi, A.; Yanai, N.; Yamada, T.; Kimizuka, N. Fast and long-range triplet exciton diffusion in metal-organic frameworks for photon upconversion at ultralow excitation power. *Nat. Mater.* **2015**, *14*, 924–930.

[9] Horcajada, P.; Chalati, T.; Serre, C.; Gillet, B.; Sebrie, C.; Baati, T.; Eubank, J. F.; Heurtaux, D.; Clayette, P.; Kreuz, C. et al. Porous metal–organic-framework nanoscale carriers as a potential platform for drug delivery and imaging. *Nat. Mater.* **2010**, *9*, 172–178.

[10] Zhang, X. J.; Ballem, M. A.; Hu, Z. J.; Bergman, P.; Uvdal, K. Nanoscale light-harvesting metal-organic frameworks. *Angew. Chem., Int. Ed.* **2011**, *50*, 5729–5733.

[11] Zacher, D.; Schmid, R.; Wöll, C.; Fischer, R. A. Surface chemistry of metal–organic frameworks at the liquid–solid interface. *Angew. Chem., Int. Ed.* **2011**, *50*, 176–199.

[12] Tsuruoka, T.; Furukawa, S.; Takashima, Y.; Yoshida, K.; Isoda, S.; Kitagawa, S. Nanoporous nanorods fabricated by coordination modulation and oriented attachment growth. *Angew. Chem., Int. Ed.* **2009**, *48*, 4739–4743.

[13] Zhao, M. T.; Wang, Y. X.; Ma, Q. L.; Huang, Y.; Zhang, X.; Ping, J. F.; Zhang, Z. C.; Lu, Q. P.; Yu, Y. F.; Xu, H. et al. Ultrathin 2D metal–organic framework nanosheets. *Adv. Mater.* **2015**, *27*, 7372–7378.

[14] Liu, C. C.; Zhang, B. X.; Zhang, J. L.; Peng, L.; Kang, X. C.; Han, B. X.; Wu, T. B.; Sang, X. X.; Ma, X. Gas promotes the crystallization of nano-sized metal-organic frameworks in ionic liquid. *Chem. Commun.* **2015**, *51*, 11445–11448.

[15] Zhao, Y. J.; Zhang, J. L.; Han, B. X.; Song, J. L.; Li, J. S.; Wang, Q. Metal–organic framework nanospheres with well-ordered mesopores synthesized in an ionic liquid/CO_2/surfactant system. *Angew. Chem., Int. Ed.* **2011**, *50*, 636–639.

[16] Li, L.; Xiang, S. L.; Cao, S. Q.; Zhang, J. Y.; Ouyang, G. F.; Chen, L. P.; Su, C. Y. A synthetic route to ultralight hierarchically micro/mesoporous Al(III)-carboxylate metal-organic aerogels. *Nat. Commun.* **2013**, *4*, 1774.

[17] Liu, Y.-R.; He, L. S.; Zhang, J. Y.; Wang, X. B.; Su, C.-Y. Evolution of spherical assemblies to fibrous networked Pd(II) metallogels from a pyridine-based tripodal ligand and their catalytic property. *Chem. Mater.* **2009**, *21*, 557–563.

[18] Xue, C. F.; Tu, B.; Zhao, D. Y. Facile fabrication of hierarchically porous carbonaceous monoliths with ordered mesostructure via an organic organic self-assembly. *Nano Res.* **2009**, *2*, 242–253.

[19] Liu, N.; Yao, Y.; Cha, J. J.; McDowell, M. T.; Han, Y.; Cui, Y. Functionalization of silicon nanowire surfaces with metal-organic frameworks. *Nano Res.* **2012**, *5*, 109–116.

[20] Lin, W. B.; Rieter, W. J.; Taylor, K. M. L. Modular synthesis of functional nanoscale coordination polymers. *Angew. Chem., Int. Ed.* **2009**, *48*, 650–658.

[21] Zhao, X.; Bu, X. H.; Wu, T.; Zheng, S. T.; Wang, L.; Feng, P. Y. Selective anion exchange with nanogated isoreticular positive

metal-organic frameworks. *Nat. Commun.* **2013**, *4*, 2344.

[22] Li, L.; Liu, X. L.; Geng, H. Y.; Hu, B.; Song, G. W.; Xu, Z. S. A MOF/graphite oxide hybrid (MOF: HKUST-1) material for the adsorption of methylene blue from aqueous solution. *J. Mater. Chem. A* **2013**, *1*, 10292–10299.

[23] Zhao, X. L.; Liu, S. L.; Tang, Z.; Niu, H. Y.; Cai, Y. Q.; Meng, W.; Wu, F. C.; Giesy, J. P. Synthesis of magnetic metal-organic framework (MOF) for efficient removal of organic dyes from water. *Sci. Rep.* **2015**, *5*, 11849.

[24] Wei, Y. H.; Dong, H. Y.; Wei, C.; Zhang, W.; Yan, Y. L.; Zhao, Y. S. Wavelength-tunable microlasers based on the encapsulation of organic dye in metal–organic frameworks. *Adv. Mater.* **2016**, *28*, 7424–7429.

[25] Chaudhari, A. K.; Han, I.; Tan, J. C. Multifunctional supramolecular hybrid materials constructed from hierarchical self-ordering of *in situ* generated metal-organic framework (MOF) Nanoparticles. *Adv. Mater.* **2015**, *27*, 4438–4446.

[26] Xin, C. L.; Zhan, H. J.; Huang, X.; Li, H. G.; Zhao, N.; Xiao, F. K.; Wei, W.; Sun, Y. H. Effect of various alkaline agents on the size and morphology of nano-sized HKUST-1 for CO_2 adsorption. *RSC Adv.* **2015**, *5*, 27901–27911.

[27] Prestipino, C.; Regli, L.; Vitillo, J. G.; Bonino, F.; Damin, A.; Lamberti, C.; Zecchina, A.; Solari, P. L.; Kongshaug, K. O.; Bordiga, S. Local structure of framework Cu(II) in HKUST-1 metallorganic framework: Spectroscopic characterization upon activation and interaction with adsorbates. *Chem. Mater.* **2006**, *18*, 1337–1346.

[28] Jeong, N. C.; Samanta, B.; Lee, C. Y.; Farha, O. K.; Hupp, J. T. Coordination-chemistry control of proton conductivity in the iconic metal-organic framework material HKUST-1. *J. Am. Chem. Soc.* **2012**, *134*, 51–54.

[29] Iler, R. K. *The Chemistry of Silica: Solubility, Polymerization, Colloid and Surface Properties and Biochemistry of Silica*; John Wiley & Sons: New York, 1979.

[30] Wei, S. C.; Pan, M.; Li, K.; Wang, S. J.; Zhang, J. Y.; Su, C. Y. A multistimuli-responsive photochromic metal-organic gel. *Adv. Mater.* **2014**, *26*, 2072–2077.

[31] Sumida, K.; Rogow, D. L.; Mason, J. A.; McDonald, T. M.; Bloch, E. D.; Herm, Z. R.; Bae, T.-H.; Long, J. R. Carbon dioxide capture in metal–organic frameworks. *Chem. Rev.* **2012**, *112*, 724–781.

[32] Kim, Y. K.; Hyun, S. M.; Lee, J. H.; Kim, T. K.; Moon, D.; Moon, H. R. Crystal-size effects on carbon dioxide capture of a covalently alkylamine-tethered metal-organic framework constructed by a one-step self-assembly. *Sci. Rep.* **2016**, *6*, 19337.

[33] Rodenas, T.; Luz, I.; Prieto, G.; Seoane, B.; Miro, H.; Corma, A.; Kapteijn, F.; Llabrés i Xamena, F. X.; Gascon, J. Metal-organic framework nanosheets in polymer composite materials for gas separation. *Nat. Mater.* **2015**, *14*, 48–55.

[34] Campbell, M. G.; Liu, S. F.; Swager, T. M.; Dinca, M. Chemiresistive sensor arrays from conductive 2D metal-organic frameworks. *J. Am. Chem. Soc.* **2015**, *137*, 13780–13783.

[35] Talin, A. A.; Centrone, A.; Ford, A. C.; Foster, M. E.; Stavila, V.; Haney, P.; Kinney, R. A.; Szalai, V.; El Gabaly, F.; Yoon, H. P. et al. Tunable electrical conductivity in metal-organic framework thin-film devices. *Science* **2014**, *343*, 66–69.

[36] Yoon, M.; Srirambalaji, R.; Kim, K. Homochiral metal-organic frameworks for asymmetric heterogeneous catalysis. *Chem. Rev.* **2012**, *112*, 1196–1231.

[37] Dhakshinamoorthy, A.; Asiri, A. M.; García, H. Metal–organic framework (MOF) compounds: Photocatalysts for redox reactions and solar fuel production. *Angew. Chem., Int. Ed.* **2016**, *55*, 5414–5445.

[38] Mahdavinia, G. R.; Aghaie, H.; Sheykhloie, H.; Vardini, M. T.; Etemadi, H. Synthesis of CarAlg/MMt nanocomposite hydrogels and adsorption of cationic crystal violet. *Carbohydr. Polym.* **2013**, *98*, 358–365.

[39] Zhu, Y.; Wang, Y. M.; Zhao, S. Y.; Liu, P.; Wei, C.; Wu, Y. L.; Xia, C. K.; Xie, J. M. Three N–H functionalized metal-organic frameworks with selective CO_2 uptake, dye capture, and catalysis. *Inorg. Chem.* **2014**, *53*, 7692–7699.

[40] Mahdavinia, G. R.; Hasanpour, J.; Rahmani, Z.; Karami, S.; Etemadi, H. Nanocomposite hydrogel from grafting of acrylamide onto HPMC using sodium montmorillonite nanoclay and removal of crystal violet dye. *Cellulose* **2013**, *20*, 2591–2604.

[41] Sun, J. W.; Yan, P. F.; An, G. H.; Sha, J. Q.; Li, G. M.; Yang, G. Y. Immobilization of polyoxometalate in the metal-organic framework rht-MOF-1: Towards a highly effective heterogeneous catalyst and dye scavenger. *Sci. Rep.* **2016**, *6*, 25595.

[42] Yang, Q. Y.; Vaesen, S.; Ragon, F.; Wiersum, A. D.; Wu, D.; Lago, A.; Devic, T.; Martineau, C.; Taulelle, F.; Llewellyn, P. L. et al. A water stable metal–organic framework with optimal features for CO_2 capture. *Angew. Chem., Int. Ed.* **2013**, *52*, 10316–10320.

[43] Howarth, A. J.; Liu, Y. Y.; Li, P.; Li, Z. Y.; Wang, T. C.; Hupp, J. T.; Farha, O. K. Chemical, thermal and mechanical stabilities of metal–organic frameworks. *Nat. Rew. Mater.* **2016**, *1*, 15018.

[44] Zhang, J.-P.; Chen, X.-M. Exceptional framework flexibility and sorption behavior of a multifunctional porous cuprous triazolate framework. *J. Am. Chem. Soc.* **2008**, *130*, 6010–6017.

[45] Salles, F.; Bourrelly, S.; Jobic, H.; Devic, T.; Guillerm, V.; Llewellyn, P.; Serre, C.; Ferey, G.; Maurin, G. Molecular insight into the adsorption and diffusion of water in the versatile hydrophilic/hydrophobic flexible MIL-53(Cr) MOF. *J. Phys. Chem. C* **2011**, *115*, 10764–10776.